Ground penetrating radar in temperate ice: englacial water inclusions as limiting factor for data interpretation

Christophe Ogier[1,2], Dirk-Jan van Manen[3], Hansruedi Maurer[3], Ludovic Räss[1,2], Marian Hertrich[3], Andreas Bauder[1,2] and Daniel Farinotti[1,2]

[1]Laboratory of Hydraulics, Hydrology and Glaciology (VAW), ETH Zurich, Zurich, Switzerland; [2]Swiss Federal Institute for Forest, Snow and Landscape Research (WSL), Birmensdorf, Switzerland and [3]Institute of Geophysics, ETH Zurich, Zurich, Switzerland

Abstract

Ground penetrating radar (GPR) has been extensively used in glaciology to infer glacier's ice thickness, liquid water content, water drainage pathways, and other properties. The interpretation of such GPR data is not always straightforward and for temperate glaciers, the signal is often affected by strong scattering and attenuation. It has often been suggested that such effects originate from englacial water inclusions, since water and ice have a large contrast in their di-electric permittivity. To investigate such effects quantitatively, we perform an extensive numerical modeling study of GPR signals. By exploring how different liquid water contents (LWC) and water-inclusions size affect the GPR signal, we show that their effects are much larger than the potential presence of a wet snowpack or a heterogeneous distribution of ice permittivity. In particularly, we show that the presence of such water inclusions is a necessary and sufficient condition for reproducing the typical characteristics of GPR data acquired in the field. Further, we find that for 25 MHz GPR antennas, a bulk LWC $\gtrsim 0.2\%$, associated with decimeters-scale water inclusions already limits bedrock detectability for ice thicknesses $\gtrsim 100$ m. Since these values are typical for Alpine glaciers, they clarify why the quality of GPR data is often poor in such environments.

1. Introduction

Ground penetrating radar (GPR) uses the electromagnetic field to infer sub-surface physical properties (Davis and Annan, 1989). GPR has been widely used in glaciology to characterize englacial structures (e.g. internal ice layers, shear zones), the glacier thermal regime, the basal topography and ice thickness, or the glacier hydrology (see Plewes and Hubbard, 2001; Woodward and Burke, 2007; Navarro and Eisen, 2009; Schroeder and others, 2020, for reviews). The detection of a target object in ice through GPR relies on measurable reflections of the propagated electromagnetic field at the object's boundaries. These reflections are essentially due to a change of relative electrical permittivity. Alternatively, diffractions can occur when the target is small compared to the frequency-dependent wavelength. In the context of detecting sub- and englacial channels, such diffracted signals are mostly unwanted and are considered as noise.

GPR is particularly suitable for cold ice studies because liquid water is minimal in such cases and most of the reflected energy is conserved and the signal absorption is limited. In contrast, the use of GPR for temperate ice is more challenging. On one hand, the permittivity contrast between ice and water is large, resulting in clear reflections from englacial water bodies. On the other hand, the presence of individual water inclusions might enhance the energy loss of the GPR signal through diffractions. Bamber (1988) demonstrated that at 60 MHz, the scattering power from englacial water bodies with a radius greater than 25 mm is larger than the scattering power from a perfectly plane boundary. This results in a strong attenuation of the reflected signals.

The last decades have seen a growing interest in GPR studies on temperate glaciers, and notable improvements on data acquisition and processing methods have been achieved (e.g. Schroeder and others, 2020). In polythermal glaciers, strong diffractions from englacial liquid water and the associated noise signal has been used to identify the cold-temperate transition surface (e.g. Björnsson and others, 1996), while in temperate glaciers it has been used to estimate the liquid water content (LWC) (e.g. Murray and others, 2000). In many cases, however, the GPR signal in temperate ice is too blurry to interpret englacial characteristics or even bedrock positions. Some of the airborne-GPR profiles discussed in Grab and others (2021), for instance, do not reveal any bedrock reflections although the same instrumental setting gave good results for other profiles with similar bedrock geometries. Similar is true for ground-based GPR measurements acquired in 2019 on the two temperate Swiss glaciers Triftgletscher and Glacier du Trient (discussed later) which only reveal bedrock reflections at very few locations, even for glacier areas where the bedrock is expected to show a shallow slope (imaging of the bedrock might be precluded for geometrical reasons in sections with steeply dipping bedrock).

Smith and Evans ([1972]) suggested that it is the presence of liquid water – rather than the ice fabrics, the impurity content, or the temperature – which is mainly responsible for the backscattered GPR signal in temperate ice. In response to Smith and Evans ([1972]), Watts and England ([1976]) recommended to use GPR frequencies below 10 MHz to limit the scattering power from englacial water bodies, for bedrock detection. However, there has been no systematic investigation on the subject so far. Although it is clear that the amount and distribution of englacial water impacts the interpretation of the GPR signal, water content variations and distribution have rarely been addressed quantitatively, rendering the interpretation of the GPR signal's 'blurriness' speculative.

Numerical modeling to emulate the GPR signal in synthetic glacial environments provides an avenue to tackle the problem, but so far, only few studies leveraged this possibility. For instance, Barrett and others ([2008]) characterized distribution and size of water inclusions from a surge-type glacier by comparing their field-based GPR results to forward modeling results. They were able to explain the observed GPR data by implementing decimeter-scale water inclusion confined in dipping planar features. Catania and others ([2008]) suggested the presence of moulins in the Greenland ice sheet from GPR measurements. They reproduced the synthetic moulin signature by numerical modeling and found a good correlation with the field-based data, thus validating their initial suggestion.

In this study, we use numerical modeling to validate the statement of Smith and Evans ([1972]) - that liquid water is mainly responsible for the back-scattered GPR signal in temperate ice - and to quantify the impact that the englacial water content has on the GPR signals. In particular, we perform a set of synthetic forward-simulations of the GPR signal, and explore the impact of changing snow thickness, ice permittivity distribution, LWC values and size of the water inclusions. Permittivity distribution, LWC and water inclusions size values are taken from field observations on temperate glaciers. Our aim is to indicate which values of water content and which size of water inclusions significantly diminish GPR reflection returns which are useful for interpretations of the GPR signal.

2. Method

2.1 Background theory

Diffraction patterns in GPR sections often appear as random, yet one would expect them to have a deterministic origin. We have three hypotheses for the origin of these patterns, namely (1) the presence of a wet snowpack at the glacier surface, (2) heterogeneous ice properties, such as variations in the ice permittivity, and (3) small-scale water inclusions which may act as distributed scatterers. We neglect the others type of inclusions such as rocks or air voids (see Section Discussion). Here, we test which of the three hypotheses is the most likely one, and do so by isolating the different cases. In the following, we refer to these three cases as 'glacier models'.

2.2 Glacier models

A glacier model is defined by its geometry and materials properties. In order to assess the effects on the GPR data, we build our glacier models upon a reference model in two dimensions, and sequentially add new features to it. More specifically, we start with a reference model consisting of homogeneous, water-free ice, and then add, in turn, (i) a snowpack with a given LWC, (ii) heterogeneous ice properties with stochastic fluctuations, and (iii) small-scale water inclusions distributed amid the ice.

Table 1. Model parameters for the forward simulations of the GPR signal

Constant parameters	Value	Remarks
Glacier width	100 m	Long enough to resolve Kirchhoff migration
Ice thickness	100 m	Flat bedrock
Subglacial channel radius	2 m	
Free parameters		
Snowpack thickness	1 m and 10 m	Fig. 1b
Ice permittivity	2.9 (–) to 3.26 (–)	Fig. 1c
Liquid water content (LWC)	0.1 % to 1.5 %	Fig. 1d
Maximal scatterer radius (r_{max})	0.1 m, 0.5 m, 1.0 m	Fig. 1d

The subglacial channel radius is considered to be a typical value (Fountain and Walder, [1998]; Cuffey and Paterson, [2010]). The maximal scatterer radius r_{max} refers to the size of the randomly distributed water inclusions.

Table 2. Di-electrical properties of the space-domain for the gprMax simulations

Material	Permittivity ϵ_r (-)	Conductivity σ (S m^{-1})
Glacier ice	2.9 to 3.26	5×10^{-8}
Bedrock (granite)	6	10^{-3}
Glacial melt water	80	5×10^{-4}
Wet snow	2.3	10^{-4}

Di-electric properties of granite and glacial melt water are taken from Plewes and Hubbard ([2001]). Di-electric properties of ice vary stochastically with values according to Jezek and others ([1978]), Johari and Charette ([1975]) and Plewes and Hubbard ([2001]). Di-electric properties of wet snow are calculated from Tiuri and others ([1984]) and Granlund and others ([2010]) with a snow density of $\rho_{snow} = 500$ kg m^{-3} and LWC = 3 %. Permeability μ and magnetic loss Ω are kept constant at $\mu = 1$ and $\Omega = 0$ Ohm m^{-1} for all materials.

All simulations share constant geometry parameters such as ice thickness and glacier width (Table 1) while the di-electrical properties of the ice are given in Table 2.

2.2.1 Reference model: homogeneous, water-free glacier ice

The geometry and materials of the reference model are given in Figure 1a. The geometry includes a flat bedrock at 100 m depth and a subglacial channel with a radius of 2 m. We include the subglacial channel as a possible target for a GPR campaign. As such, the bedrock and the subglacial channel represent the two targets for which we will check how the imaging quality is affected by the model additions presented below.

2.2.2 Model addition 1: wet snowpack at the glacier surface

Glacier ice is often overlain by snow or firn, and this layer might contain some liquid water. Such conditions are particularly prominent in spring, when GPR campaigns are often performed (e.g. Bauder and others, [2018]). We assess the impact of such a layer by adding it to the surface of our reference model (Fig. 1b). The layer thickness is either 1 m or 10 m, which we consider being the range of a typical snowpack in Alpine settings. We calculate the layer's permittivity ϵ_s by using the parametrization suggested by Tiuri and others ([1984]):

$$\epsilon_s = (0.1\,LWC + 0.8\,LWC^2)\epsilon_w + \epsilon_d, \qquad (1)$$

where 0.1 and 0.8 are two empirically determined coefficients, LWC is the liquid water content, $\epsilon_w = 80$ is the relative permittivity of the water (Table 2), and ϵ_d is the relative permittivity of dry snow. The latter is calculated from the density ratio between snow and water, that is ρ_{snow}/ρ_w (dimensionless):

$$\epsilon_d = 1 + 1.7 \times \rho_{snow}/\rho_w + 0.7 \times (\rho_{snow}/\rho_w)^2. \qquad (2)$$
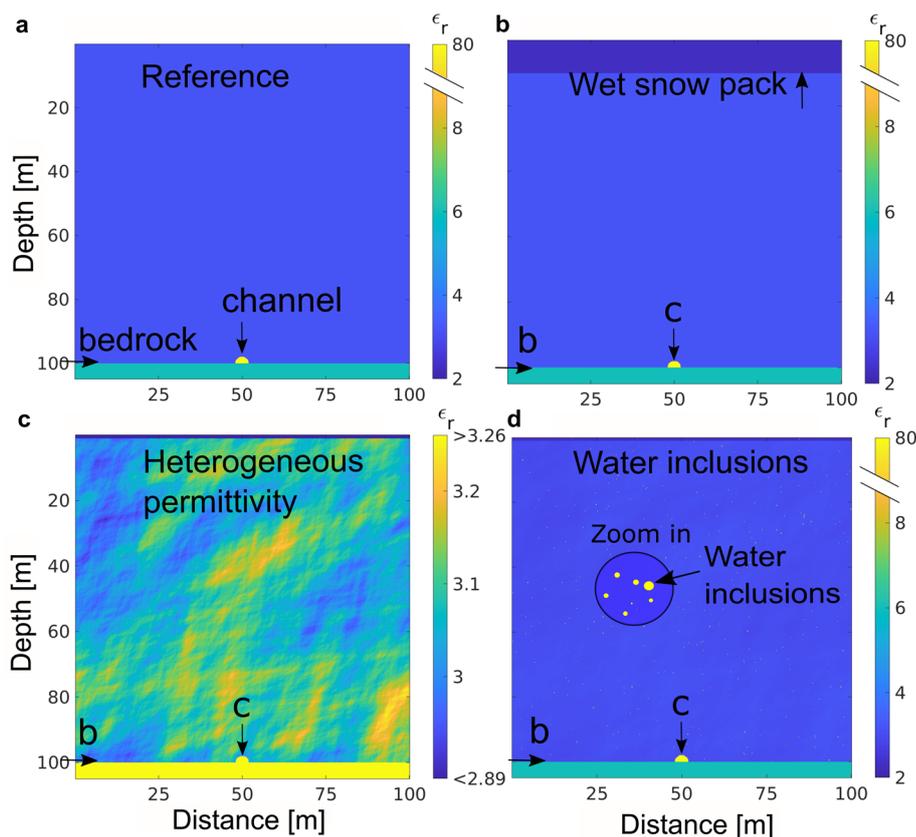
Figure 1. 2D geometry of the investigated glacier models and relative permittivity (ϵ_r) for (a) the reference model, (b) the additional wet snowpack, here 10 m thick, (c) the additional stochastic variation of ice permittivity (note the different color scale), and (d) the additional water inclusions (here $LWC = 0.2\%$ and $r_{max} = 0.1$ m). The position of the bedrock (labeled 'b') and the subglacial channel (labeled 'c') are indicated by arrows for each model.

The wet snow conductivity σ (μS m^{-1}) is calculated following Granlund and others (2010):

$$\sigma \approx 10 + 3 \times 10^3 \, LWC. \tag{3}$$

With the above equations, a typical spring snowpack over glaciers with $\rho_{snow}/\rho_w = 0.5$ and $LWC = 3\%$ (Griessinger and others, 2018), results in $\epsilon_s = 2.3$ and $\sigma = 10^{-4}$ S m^{-1}. These values are in good agreement with field observations (see e.g. Fig. 5 in Evans (1965)). Note that the value for ϵ_s is close to the permittivity of ice (see Table 2), and that we consider a bulk permittivity for the snowpack, i.e. we do not explicitly account for the snowpack's water inclusions. Our argument for doing so is that these water inclusions are expected to be very small when compared to the wavelength of the GPR signal in snow: at 25 MHz, the latter is in the order of 1 m, while the diameter of the water inclusions in snow are expected to be <1 mm (e.g. Coleou and others, 2001). Moreover, we also ignore stochastic variations in permittivity that could occur because of a heterogeneous distribution of water content. We deem this omission to be acceptable after testing the effect that such a stochastic permittivity distribution would have in a 10 m thick snow pack (not shown) and after ascertaining that the effect is not large enough as to mask the strong diffraction patterns that we typically see in the field data and that we try to explain.

2.2.3 Model addition 2: heterogeneous ice permittivity
Measurements of the relative permittivity of ice ϵ_r (dimensionless) range between 2.89 and 3.26, with a mean value of ~3.2 (Robin and others, 1969; Johari and Charette, 1975; Jezek and others, 1978; Plewes and Hubbard, 2001; Reynolds, 2011; Bohleber and others, 2012). Variations in ϵ_r occur due to the permittivity's dependence on ice density, temperature, and crystal orientation fabrics. The influence of ice density is discussed in Kovacs and others (1995), who proposed a slightly modified

relationship proposed by Robin and others (1969) for capturing such effects.

Ice density in alpine glaciers is most often considered to be homogeneous, and we thus expect ϵ_r to vary only slightly. Bohleber and others (2012), for example, reported variations in the order of a few percent (see their Fig. 4). Crystal orientation fabrics can also influence ϵ_r, with variations in the order of 1% (Johari and Charette, 1975; Fujita and others, 1993).

Here, we account for the natural variations in ice permittivity by imposing stochastic variations on ϵ_r in the range of 2.89 to 3.26 (Fig. 1c). The stochastic distribution is parameterized with a von Karman type correlation function (Goff and Holliger, 2012) described by a Hurst number 0.5 (that is an exponential distribution) and a correlation length of 10 m (both in the horizontal and the vertical dimension). The Hurst number (also known as the 'fractal dimension') characterizes the amount of heterogeneity in a natural medium (Goff and Holliger, 2012), and we will explore the sensitivity of this value in the Results section.

2.2.4 Model addition 3: scattering water inclusions
Water inclusions are modeled as randomly distributed, spherical scatterers. We constrain LWC and the size of the scatterers based on literature values. Barrett and others (2008) explain strong scattering in a surging glacier by the presence of water inclusions of multi-decimeter scale. Likewise, Hodge (1976) observed englacial voids in boreholes, reporting that typical vertical extents were of several decimeters (see their Fig. 3).

LWC in temperate ice has been estimated from GPR by analyzing the electromagnetic wave velocity (Macheret and others, 1993; Moore and others, 1999; Murray and others, 2000) or from the back-scattered power in individual GPR sections (Bamber, 1988; Hamran and others, 1996; Macheret and Glazovsky, 2000). Reported LWC values ranges from 0.5% to 1.5% in Murray and others (2000), from 0.3% to 1.7% in Raymond and

Harrison ([1975]); Vallon and others ([1976]), and from 0 % to 9 % in Pettersson and others ([2004]).

More recently, LWC has been estimated from surface nuclear magnetic resonance (SNMR). SNMR is a geophysical technique that allows the direct detection and quantification of liquid water in the subsurface. It takes advantage of the magnetic moment and spin of the hydrogen nuclei of water. Traditionally applied in hydrological applications, the technique has shown promising results in glacier applications too (e.g. Hertrich and others, [2007]; Legchenko and others, [2011]; Garambois and others, [2016]). In summer 2008, SNMR was for example performed at the tongue of Rhonegletscher, a temperate glacier in Switzerland, yielding an average LWC estimates of 0.8 % ± 0.4 % for the sampled vertical profile (Hertrich and Walbrecker, [2008]).

To test the effect of different configurations of distributed scatterers on the GPR signals, we perform simulations in which we (i) vary the LWC between 0.1 % and 1.5 %, with increments of 0.1 % (i.e. fifteen different values for LWC) and (ii) randomly vary the radius of the water inclusions between 0 and a maximal radius of either $r_{max} = 0.1$ m, $r_{max} = 0.5$ m, or $r_{max} = 1.0$ m. This results in a total of $15 \times 3 = 45$ simulations ([Fig. 1d] provides one example). The position of the scatterers is randomly generated but remains the same for each combination of LWC and r_{max}. This is to allow for comparisons between simulations. The di-electric properties of the water inclusions are the ones of glacial melt water (see [Table 2]).

2.3 Numerical modeling and processing of GPR data

2.3.1 Modeling algorithm

For modeling the GPR signal numerically, we use the open source software gprMax (Warren and others, [2016]). gprMax implements Yee's algorithm to solve Maxwell's equations in 2D or 3D using the finite-difference method in the time-domain (FDTD, Kunz and Luebbers, [1993]). Here, we use the 2D configuration, for which gprMax uses the so-called transverse magnetic mode. This is achieved by setting the length of one of the horizontal dimensions to the spatial discretization, thus reducing that dimension to a single grid point. We use this 2D modeling approach (as opposed to 3D) because GPR field-data are most often migrated in 2D profiles and to reduce computational cost.

The source signal in gprMax is set to a Hertzian dipole with a dominant frequency of 25 MHz (a typical frequency for investigations on Alpine glaciers; e.g. Church and others, [2020]; Grab and others, [2021]) and with a Ricker type source-time function. To mimic field measurements, we place the transmitter and receiver antennas at 0.5 m above the glacier surface and perpendicular to the investigated profile. The spacing between the transmitter and the receiver is kept constant at 4 m (corresponding to one wavelength in air at 25 MHz). The spatial increment of the antennas position along the profile (i.e. the trace spacing) is of 0.5 m. The length of the GPR profile for each simulations is 95 m and corresponds to 190 traces. gprMax antennas characteristics are summarized in [Table 3].

In order to run the gprMax simulations, we discretize the glacier models defined in the previous Section in space and time. To avoid numerical dispersion, the space discretization length Δl should be $\leq \lambda_{min}/10$ (Warren and others, [2016]), where λ_{min} is the smallest wavelength of the propagating electromagnetic field. For a given frequency, λ_{min} is associated to the material with the smallest electromagnetic propagation velocity v_{min}. We calculate λ_{min} as follows:

$$\lambda_{min} = \frac{v_{min}}{f_{max}} = \frac{c}{3f\sqrt{\epsilon_r}}, \qquad (4)$$

Table 3. Time and space parameters for the gprMax simulations

gprMax antenna characteristics	Value	Remarks
Frequency	25 MHz	
Waveform type	Ricker	Amplitude =0.99
Antenna dipole	Hertzian	
Antenna separation	4 m	
Antenna step size	0.5 m	
Antenna height above surface	0.5 m	
Antenna orientation		Perpendicular to profile
gprMax time/domain parameters		
GPR profile length	95 m	190 GPR traces
Cell size (Δl)	0.05 m	Frequency dependant
Time step	1.05×10^{-10} s	Frequency dependant
Time window	1.5×10^{-6} s	Two-way travel time
Perfectly match layer width	10 cells	Absorbing layer

where ϵ_r is the relative permittivity and f the central frequency ($f_{max} = 3 \times f$ as we consider as null the amplitude beyond three times the central frequency for a Ricker waveform). In our case, λ_{min} is found for water, which is the material with the largest relative permittivity (see [Table 2]) and thus the smallest velocity ($v_{water} = 0.33 \times 10^8$ m s^{-1}).

For $f = 25$ MHz and water, λ_{min} is 0.44 m, and we thus chose $\Delta l = 0.05$ m. This allows to speed up the simulations compared to $\Delta l = 0.05$ m by a factor of 5 (more information on computational time follows below). This means that the wavelength in the water is sampled by nine cells. The fact that we sample by nine cells instead of ten means that the highest frequency (and thus the shortest wave length) propagates with a velocity on the grid that is 0.93 % smaller than the desired velocity (Schneider, [2010]) – a difference which we consider as being negligible. The time is discretized according to Δl and following the Courant-Freidrichs-Lewy stability condition (Warren and others, [2016]). The receiver recording time is set to 1.5×10^{-6} s, which corresponds to a penetration depth of the signal in ice of ~125 m (two-way travel time). A so-called perfectly matched layer width of ten cells (i.e. 0.5 m) is set on the model boundaries to absorb the signal and simulate an unbounded space (Berenger, [1996]). Time and space model parameters for gprMax are summarized in [Table 3].

Solving Maxwell's equations using the FDTD approach for high-resolution data is computationally expensive. To accelerate the simulations, we run gprMax on graphics processing units (GPUs). The FDTD discretization allows for a natural and efficient parallelization of the solver and allows leveraging the parallel processing capabilities of latest GPUs. We run the simulations using eight Nvidia A100 (SXM4, 40GB) GPUs. gprMax also allows for multi-GPU configurations, where independent trace computations are distributed among GPUs using message passing interface for distributed parallelization in a master-slave configuration. GPU computing permitted to speed up the simulations by a factor of 15 compared to multi-threaded central processing unit configurations. This results in a typical runtime for a single simulation of ~5 min. All data necessary to reproduce our gprMax simulations, including the MATLAB input files generator, are available in the Section Code and Data Availability.

2.3.2 GPR data processing

The gprMax output contains time series of the electromagnetic field strength for all grid cells and for all traces. As for field data, further processing is required to generate GPR sections that can actually be interpreted. For this, we employ our in-house Matlab-based toolbox GPRglaz (Grab and others, [2018]) and follow the processing workflow typically used for field-based investigations (e.g. Church and others, [2020]; Grab and others, [2021]).

More specifically the workflow comprises (1) time zero correction based on the arrival of the direct wave, (2) bandpass filtering (10 MHz to 65 MHz) to cut undesirable low and high frequencies generated by numerical dispersion, and (3) image focusing and time-to-depth conversion that migrates the data with a constant radar wave velocity (0.167 m ns^{-1} for ice; Glen and Paren, 1975). Migration is performed with a Kirchhoff time migration scheme (Margrave and Lamoureux, 2019). For access to the generated GPRglaz results, see the Section Code and Data Availability.

3. Results

3.1 Impact of a wet snowpack (model addition 1) and a heterogeneous ice permittivity (model addition 2)

Figures 2a, 2b and 2c present the GPR-signals from our gprMax simulations for the reference model (i.e. homogeneous ice), the additional wet snow pack at glacier surface, and for the additional stochastic distribution of ice permittivity, respectively (see also Fig. 1). Early times carry the signature of the direct wave traveling from the transmitter to the receiver antenna. The bedrock reflection is clearly visible, and the channel structure manifests itself in form of an X-shaped pattern. This is an artifact from the Kirchhoff migration, which is due to its diffraction-limited characteristic (Özdemir and others, 2014).

The snowpack at the glacier's surface has no visible influence on the signal, even when it has a thickness of 10 m (see Fig. 2b). This is in agreement with Smith and Evans (1972), who stated that GPR signal attenuation of wet snow is relatively small as long as the liquid water is salt-free – a condition certainly met in Alpine environments.

A heterogeneous ice permittivity results in small perturbations of the signal (Fig. 2c). However, the strength of the signals is significantly weaker than the one reflected from the bedrock and the subglacial channel. The statement holds true also when varying the parameters that govern the stochastic distribution of the permittivity (these are the Horst number v and the correlation length λ): Fig. 3 shows the results for simulations with $v = 0.1$ and $v = 2$, as well as $\lambda = 1$ m and $\lambda = 20$ m – a range of values that we assume cover any plausible variations in real-world conditions. Both the resulting field strengths and noise patterns are very similar to Fig. 2c, indicating that the choice of model parameters and, more importantly, of variations in permittivity as such, only have a marginal influence on the retrieved GPR signal.
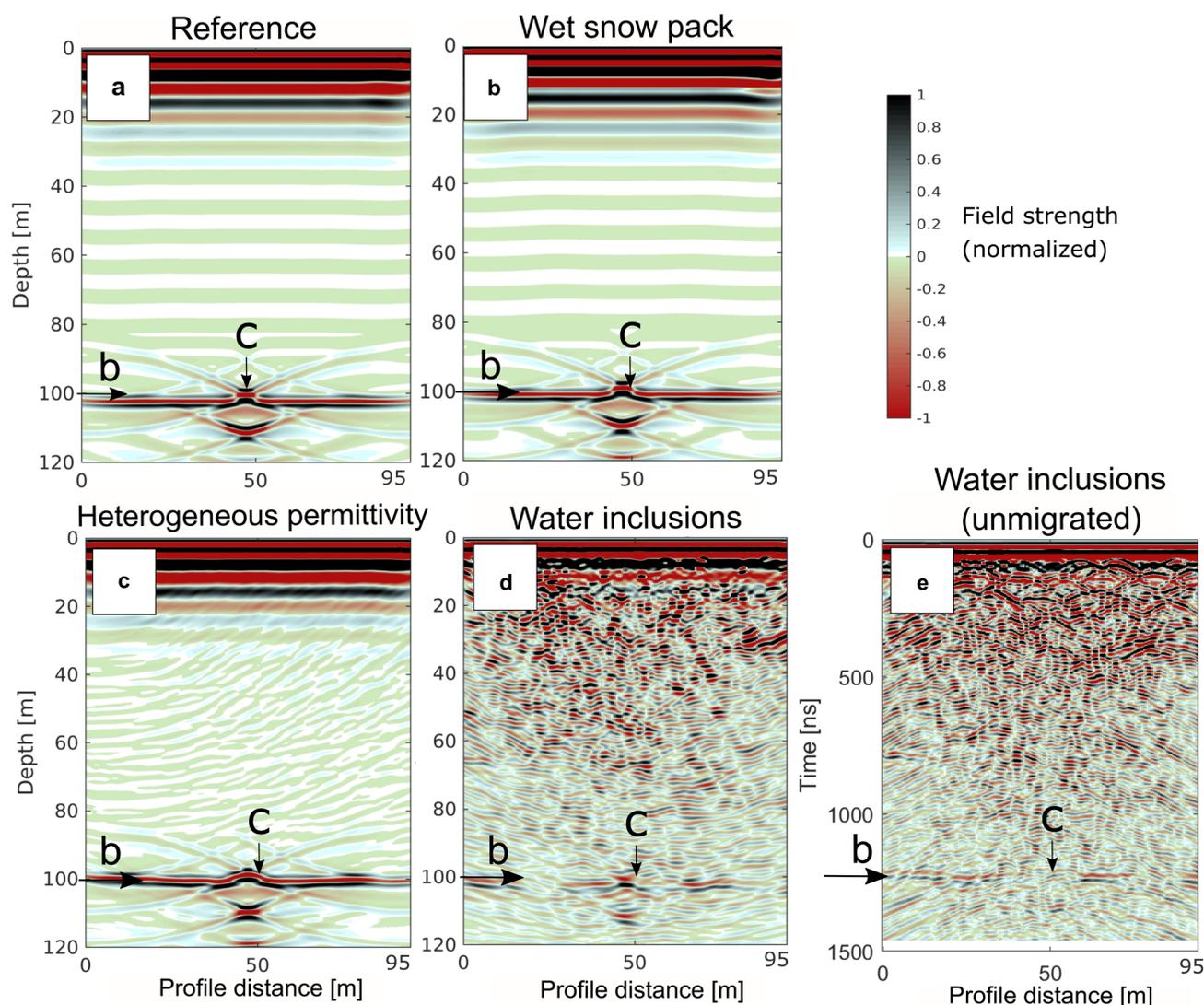
Figure 2. Results of the gprMax simulations for the (a) reference model, (b) additional wet snowpack, here 10 m thick, (c) additional stochastic variation of ice permittivity, and (d) and (e) additional water inclusions (here $LWC = 0.1\%$ and $r_{max} = 0.1$ m). The associated geometry and materials are shown in Figure 1. The positions of the bedrock (label 'b') and the subglacial channel (label 'c' are indicated by arrows for each model. All Results are presented for a frequency of 25 MHz. Results (a),(b),(c) and (d) are presented after Kirchhoff migration, and (e) is presented before Kirchhoff migration (time in y-axis).
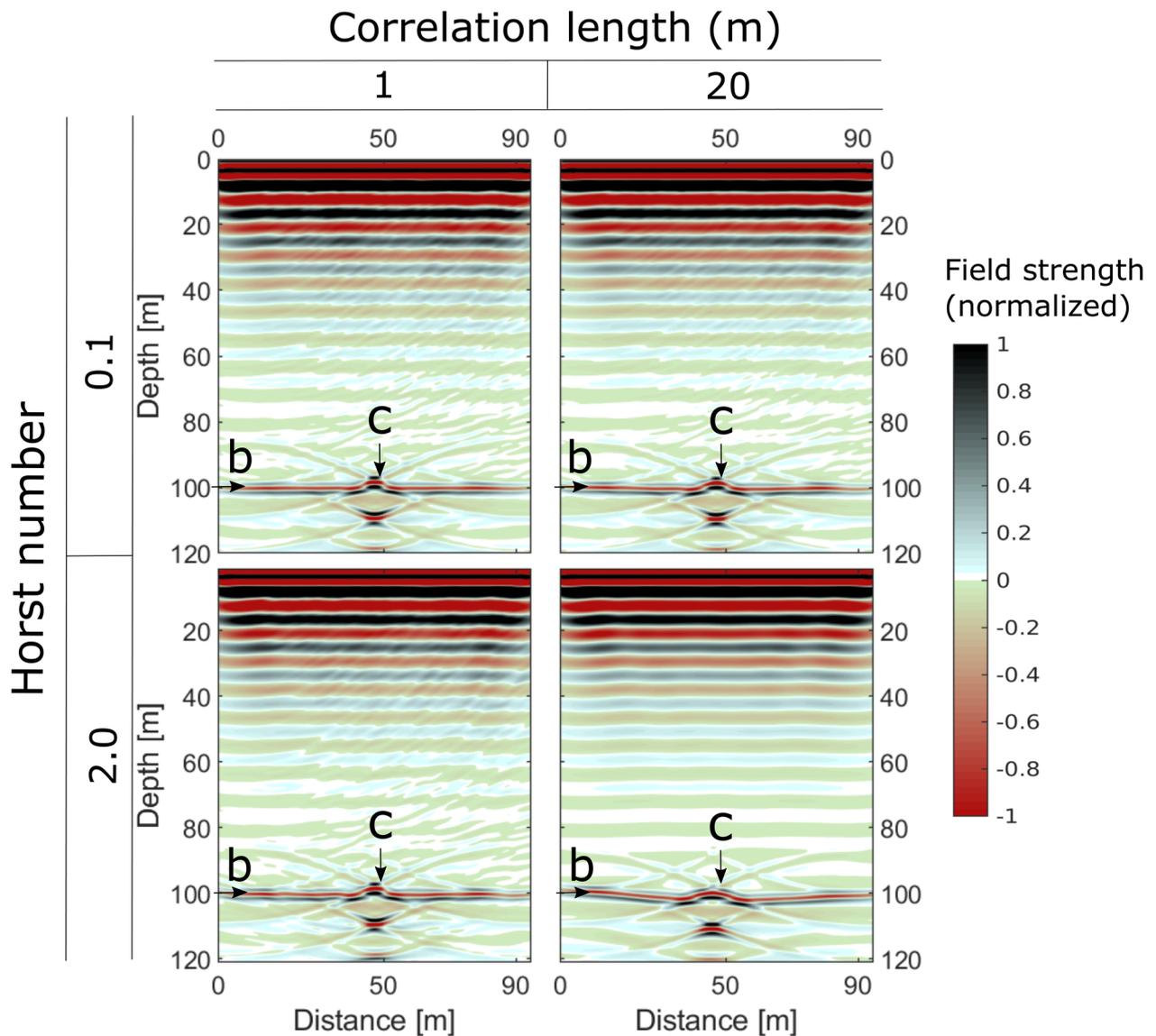
Figure 3. Sensitivity test for the Horst number ν and the correlation length λ used for simulating a stochastic distribution of ice permittivity. The range of explored values (i.e. $\nu = [0.1, 2.0]$ and $\lambda = [1, 20]$ m) are considered to be plausible upper- and lower-bounds. Data are presented after Kirchhoff migration. The bedrock (label 'b') and the subglacial channel (label 'c') are indicated.

We thus conclude that natural variations in ice permittivity are insufficient to explain the noise that characterizes many GPR data acquired in the field for temperate glaciers.

3.2 Impact of water inclusions (model addition 3)

The impact of water inclusions on the GPR signal is shown in Fig. 2d, and results in a signal that is qualitatively similar to field data (see the Discussion Section for more details). For the chosen parameters (i.e. $LWC = 0.1\%$, $r_{max} = 0.1$ m), the bedrock and the subglacial channel remain visible, although much less clearly than for the reference model. Fig. 2e presents the unmigrated GPR signal for $LWC = 0.1\%$ and $r_{max} = 0.1$ m too. The unmigrated signal shows more clearly the detrimental effect of the water inclusions on the bedrock and the subglacial channel detectability, which is partially improved by the Kirchhoff migration.

To further investigate the effects of water inclusions, the simulations are repeated with different LWCs and different sizes of the water inclusions. Figure 4 presents a selection of simulation for three values of each LWC and maximum scatterer radius. In all

cases, the GPR signal is strongly attenuated with increasing depth because of the energy lost through scattering. For $LWC = 0.1\%$ and $r_{max} = 0.1$ m, the bedrock and the subglacial channel are clearly visible. For higher LWC (e.g. 0.5% and 1%), the bedrock and the subglacial channel are no longer visible, regardless of the radius of the water inclusions. This indicates that bulk LWC values in the range of 0.1% – 0.5%, associated to water inclusions with radii in the order of several decimeters, already constitute a limit beyond which a bedrock at 100 m depth becomes impossible to detect with a frequency of 25 MHz. When the scatterer size increases for a constant LWC (i.e. when the number of scatterers decreases), more sections of water-free ice appear between the surface and the bedrock. In these sections, the bedrock is more visible, as seen when comparing the results with $r_{max} = 1$ m and $r_{max} = 0.5$ m in Fig. 4. Also note that the bedrock depth tends to be slightly overestimated with increasing LWC. This is because our Kirchhoff migration ignores the presence of water, i.e. it applies the same velocity of propagation for the electromagnetic field for all materials.

While the results presented so far refer to GPR data collected with 25 MHz antennas, we note that using different
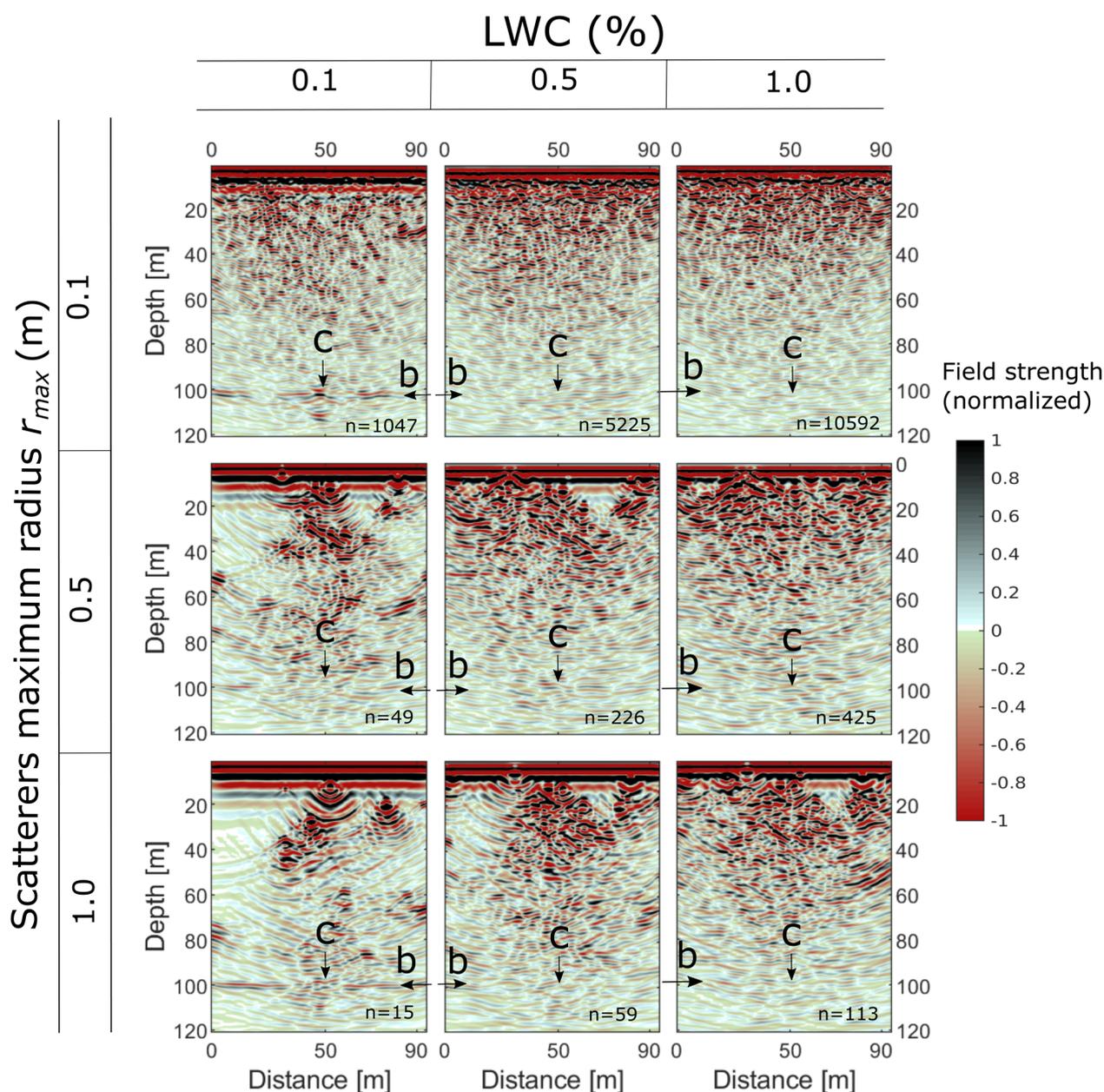
Figure 4. Results from gprMax simulations for nine combinations of LWC and maximal radius of the water inclusions. The number of individual scatterers *n* is indicated on the bottom right of each panel. The bedrock (label 'b') and the subglacial channel (label 'c') are indicated by arrows. Results refer to 25 MHz and are presented after Kirchhoff migration.

frequencies would qualitatively lead to the same results as long as the size of the scatterers are scaled with the dominant wavelength. For example, using 50 MHz and scatterers with a radius of 0.5 m would give the same results as for 25 MHz and a radius of 1.0 m. At most, a difference is expected to emerge in the achievable penetration depth and the size of the identifiable features – with higher frequencies having stronger attenuation but better spatial resolution than lower frequencies (see, e.g. Watts and England, 1976, for the spectral response of scatters according to their sizes and the frequency). When the wavelength of the electromagnetic signal in water is significantly smaller than the scatterer radius, one would also expect the appearance of multiple internal reflections. For 25 MHz and 50 MHz, this is the case for scatterers with $r_{max} > 1$ m and $r_{max} > 0.5$ m, respectively. We provide in the Section Code and data availability the additional simulations using 50 MHz for $r_{max} = 0.1$ m, $r_{max} = 0.5$ m, and $r_{max} = 1.0$ m.

4. Discussion

4.1 Similarities of synthetic and field-data

Limited bedrock detectability has often been reported (e.g. Langhammer and others, 2017; Grab and others, 2021; Rutishauser and others, 2016; Bradford and others, 2009). Figure 5a and 5b present two GPR sections acquired in August 2021 on Glacier du Trient (Switzerland), and in July 2021 on Triftglestcher (Switzerland's Mattertal), respectively. Both glaciers are temperate, and the surveys were carried out with 25 MHz antennas. The GPR data were processed with GPRglaz using the same steps as described for the gprMax simulations.

For both the mentioned GPR sections, signal scattering is particularly pronounced at depths between 20 m and 60 m. The strong bedrock is clearly visible at depths between 70 m and 100 m for Glacier du Trient and between 110 m and 130 m for Triftgletscher, but the signal is not continuous across the profiles. Figure 5c presents one of the synthetic GPR sections, generated
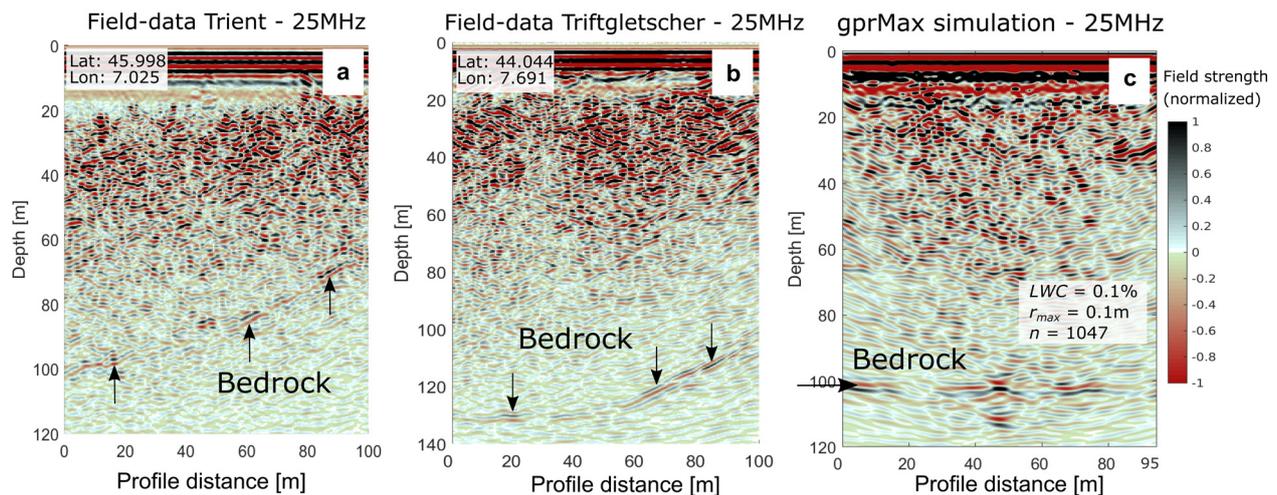
Figure 5. Comparison between real-world GPR data and data simulated through numerical modeling. Field data are shown for (a) Glacier du Trient and (b) Triftgletscher (Mattertal), two temperate glaciers in Switzerland. The data simulated with gprMax (c) are obtained with $LWC = 0.1\%$ and $r_{max} = 0.1$ m, resulting in $n = 1047$ individual scatterers. The bedrock is indicated by black arrows. All three example refer to 25 MHz antennas and are presented after Kirchhoff migration.

with gprMax with $LWC = 0.1\%$ and $r_{max} = 0.1$ m (same configuration as in Fig. 4 and same geometry as in Fig. 1d). The spatial pattern of the scatterers and the strength of the reflected energy are very similar to the real-world data shown in Fig. 5a and 5b. This similarity is only achieved when water inclusions are included in our numerical simulations, meaning that the variations in ice permittivity and the presence of a snowpack are not sufficient to reproduce the signal characteristics observed in actual field data.

4.2 Scatterer distribution within the glacier body

A simplification of our analyses is that the scatterers are distributed homogeneously in the entire glacier body. In reality, this might be different. It is known, for example, that the water level within a glacier can fluctuate in space and time as a response to pressure changes in the subglacial drainage system (e.g. Iken and others, 1996; Werder and others, 2010; Rada and Schoof, 2018; Gräff and Walter, 2021). In such cases, one would expect the scattering water inclusions to be preferentially located below an englacial water table.

Such a distribution is suggested, for example, by a second GPR section collected at Triftgletscher (Fig. 6). At horizontal distances between 0 and 450 m, the uppermost 30 m of the ice show an almost scatter-free, transparent zone (note that the some parts of this zone are partially obscured by remnants of the direct wave) while below that level, pronounced scattering is visible. Interestingly, the amount of scattering varies horizontally: between about 300 and 450 m horizontal distance, for example, the scattering decreased significantly, and as a consequence, the bedrock is clearly recognizable up to a depth of ~ 170 m. This is in contrast to the GPR section between 0 and 300 m horizontal distance, where strong scattering obscures the bedrock.

We speculate that high amounts of scattering occur for ice sections with high LWC, e.g. in areas where englacial fracturing is more pronounced due to extensional strain (Bradford and others, 2009) and where the resulting englacial voids are filled with water. To support this conjecture, we perform another set of numerical simulations in which we subdivide the ice column in two layers: an upper layer with no scatterers (i.e. $LWC = 0\%$) and a lower layer, containing all the scatterers. Results for $LWC = 0.2\%$ and $r_{max} = 0.1$ m are presented in Fig. 7. A LWC of 0.2% is chosen because the bedrock reflections already start to be obscured in this case (see Fig. 4) and because our interest is in exploring

the limits of detectability of both the bedrock and the subglacial channel.

For this two-layer configuration, the reflections stemming from both the bedrock and the subglacial channel are qualitatively similar to the one-layer case. We suggest that the reflected signal attenuation is more sensitive to LWC and scatterer-size than to the distribution of the layering. This supports the interpretation that the noisy patches often observed in field data correspond to regions with dense scatterers, the latter being in turn an expression for locally high LWC values.

The change between regions of weak and strong scattering has been often interpreted as a transition between cold and temperate ice (e.g. Blatter and Hutter, 1991; Björnsson and others, 1996; Moore and others, 1999; Gusmeroli and others, 2012). This is consistent with the interpretation provided above, as cold ice is expected to have only very low LWC and thus only very few and small water inclusions that could produce scattering. However, we note that scatter-free ice section found for Triftgletscher (Fig. 6) is temperate, not cold (this information is derived from an in-situ temperature measurement (not shown) that we conducted in the middle of the shown profile at 15 m depth during August to September 2021). We therefore suggest that temperate ice with very low LWC can have a similar GPR-signature to cold ice. In turn, this indicates that the precise characterization of the thermal regime of a glacier from GPR data alone could be more challenging than assumed so far. This interpretation is in line with findings presented by Campbell and others (2012) and, more recently, by Gerbi and others (2021).

4.3 Interpretation of the LWC variations with depth

The observations made in Fig. 6 (low scattering near the surface and much more pronounced scattering at depth) have been made on a number of other temperate glaciers too (see, e.g. Rutishauser and others, 2016, and references therein). Rutishauser and others (2016) denoted these features as 'internal reflection bands' (see their Fig. 13).

Our hypothesis is that such differences in scattering are caused by small-scale water inclusions and by LWC variations with depth. This hypothesis is not only supported by the striking similarity between our modeling results and field data (see previous Section) but also by independent field observations. Indeed, the already mentioned SNMR measurements performed on Rhonegletscher in 2008 (Hertrich and Walbrecker, 2008), indicate
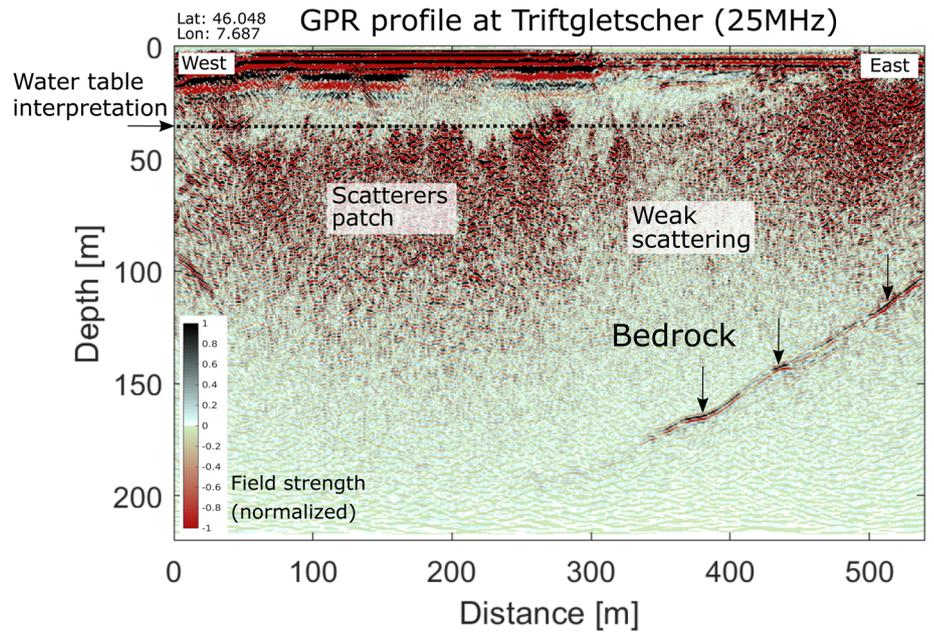
Figure 6. GPR field data after Kirchhoff migration on Triftglestcher (July 2021). The depth of the interpreted water table is marked by the horizontal dotted line above the scatterers.

such LWC variations, with $LWC \sim 0.3\%$ at 30 m below the surface and $LWC > 1\%$ below ~ 60 m.

A qualitatively similar LWC-profile was found by Bradford and others (2009) for a temperate Alaskan glacier. By analyzing GPR velocity profiles, they distinguished two distinct ice layers: a ~ 20–30 m thick layer with LWC between $\sim 0\%$ and 0.5% near the surface, underlain by a layer with LWC of $\sim 1\%$ to 2.5% (see their Fig. 6).

Also, Murray and others (2000) found a layered LWC structure for a temperate Icelandic glacier. Their Fig. 8 shows LWC $\sim 0.2\%$ at the surface and a sharp increase to $\sim 3.5\%$ at 28 m depth. Conversely to our Rhone data, however, Murray and others
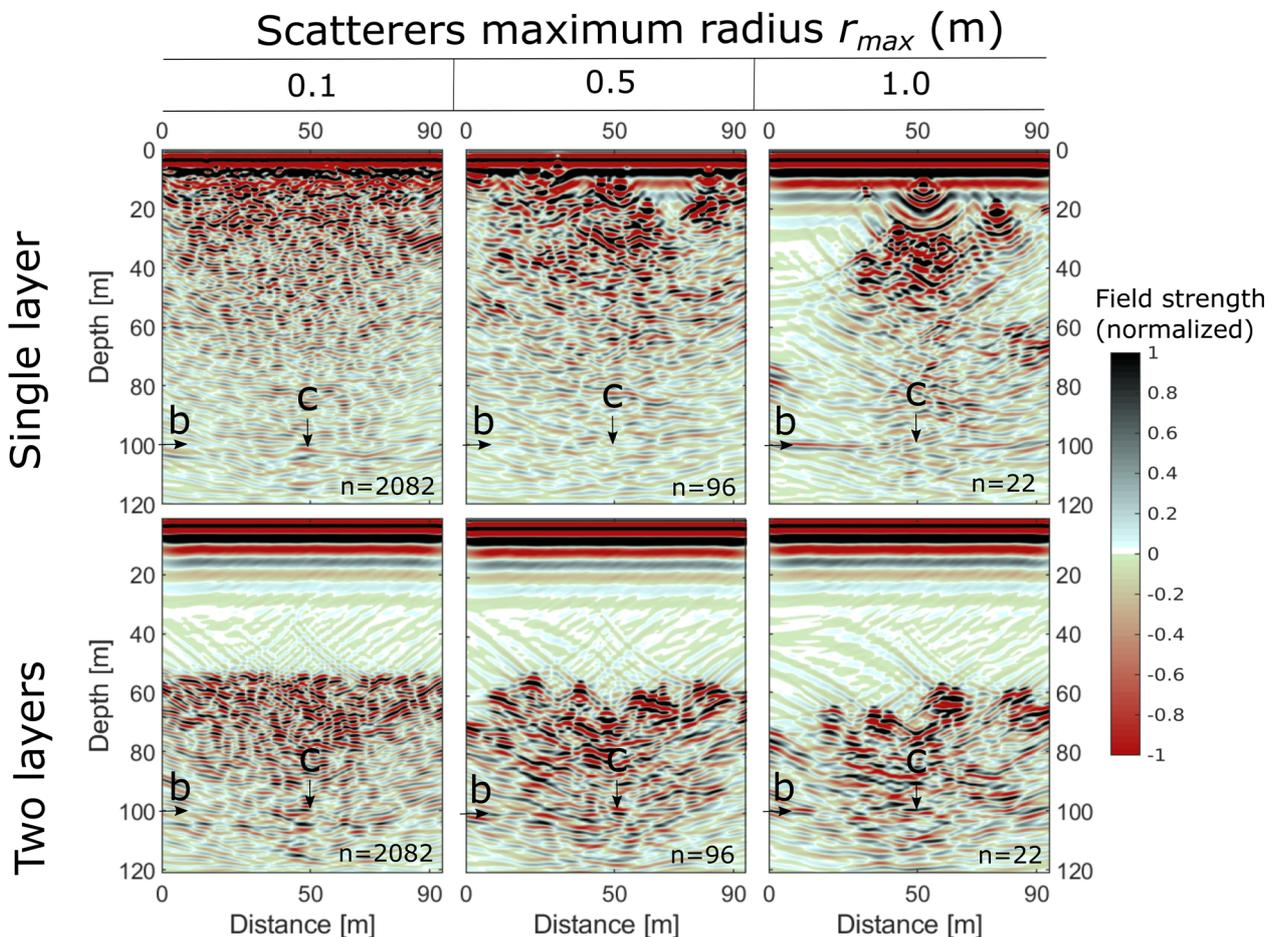
Figure 7. gprMax results for scatterers distributed (a) along the entire ice column (labeled 'single layer') and (b) only in the lower half of the ice column (labeled 'two layers'). $LWC = 0.2\%$ for all simulations. The number of scatterers n is indicated at the bottom right of each panel. The bedrock and the subglacial channel are indicated by the arrows with labels 'b' and 'c', respectively.
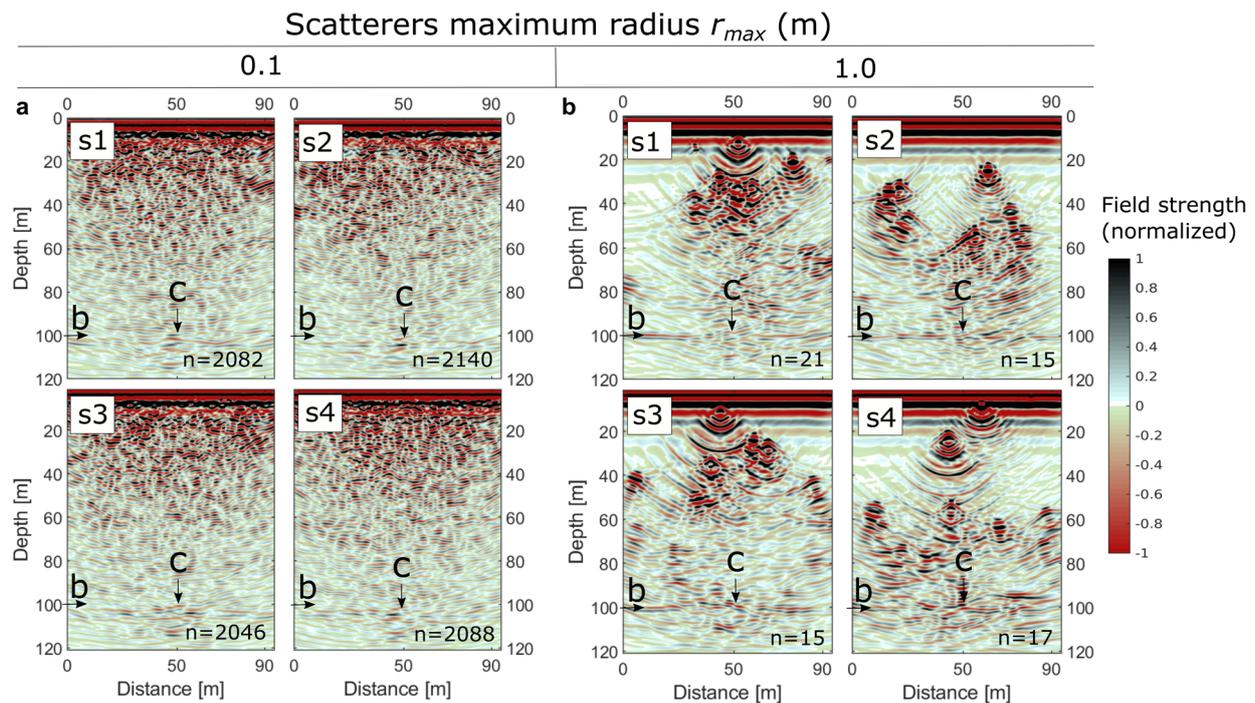
Figure 8. Sensitivity test for four different distribution of scatterers (s1 to s4). All panels have *LWC* = 0.2 % while the radius of the scatterers is either (a) r_{max} = 0.1 m or (b) r_{max} = 1.0 m. The number of scatterers *n* is approximately the same for all cases (indicated at the bottom right of each panel) while the location of the scatterers is randomly varied. The bedrock and the subglacial channel are indicated by the arrows with labels 'b' and 'c', respectively.

(2000) found that the LWC decreases again with increasing depth, until reaching ~0.1 % at the bedrock.

While the field methodologies mentioned above do not allow identifying sharp transitions in LWC, we suggest that these marked LWC changes can be interpreted as indicative for the presence of a 'water table,' i.e. a feature similar to what is found for aquifers. In this scenario, ice fractures and other voids that are present below a certain depth would be water filled, while similar features above that level would be filled with air. This interpretation is broadly consistent with observations performed during drilling campaigns on temperate glaciers: boreholes drilled in temperate glaciers generally fill with water up to a certain level, that level being in hydrostatic equilibrium with the subglacial drainage system (e.g. Iken and others, 1996; Pohle and others, 2022). With this interpretation, the finding by Murray and others (2000) (i.e. the fact that LWC decreases again close to the bedrock) could be explained by the fact that the ice overburden pressure increases with depth, thus tending to re-close any voids that might emerge.

4.4 Plausibility of the size of the water inclusions

In our simulations, we chose to limit the maximal radius of the water inclusions to r_{max} = 1 m. For one, this choice allowed for obtaining a GPR signal that is qualitatively similar to real-world GPR data. For another, these dimensions are broadly compatible with indications found in the literature.

Holmlund (1988), for example, visually observed former water-filled pockets visible at the surface of a polythermal glacier in Sweden after the surface melted out. Fig. 8 and 9 of that publication suggest that these water-filled pockets can be several meters large.

Bradford and others (2009), as another example, performed GPR velocity analysis in a temperate Alaskan glacier to infer its LWC. They concluded that most of the englacial water is likely to be contained within voids having dimensions in the order of a few centimeters up to several meters, rather than at the ice grain boundaries.

Further literature examples are difficult to find, and we thus affirm that the question about the size and number of water-filled voids in temperate glaciers merits further attention.

4.5 Influence of scatterer distribution and ice permittivity

So far, the spatial distribution of the scatterers was kept unaltered. This allowed direct comparison of the different simulations. Here, we address the sensitivity of our results to the scatterer distribution by running four gprMax simulations with *LWC* = 0.2 % and r_{max} = 0.1 m but by changing the scatterer locations. All models have a comparable number of scatterers, although the number is not exactly the same since the radii of the scatterers are randomly varied too. We call the four generated distributions 's1' to 's4' (Fig. 8).

Fig. 8a suggests that for a large number of scatterers, the spatial distribution has little impact on the signal. This is because the scattering is strong everywhere. When the LWC is small and/or scatterers are large (i.e. when scatterers are sparse), we observe a higher sensitivity of the distribution on the signal noise (Fig. 8b). Strong and uniform noise in the GPR signal is thus most likely due to a large number of relatively small scatterers.

4.6 Limitations of the method and neglected factors

Strictly speaking, the detection and imaging of isolated englacial features would require a 3D approach including a dense grid of GPR profiles. This is because side reflections from off-plane scatterers also affect the GPR signal – a situation that is neglected when applying a 2D migration (e.g. Barrett and others, 2008). Although we ignored such effects in our study, the fact that our results look very similar to field data (Fig. 5) indicates that the first-order effect of water inclusions was sufficiently captured. Our main conclusion is, thus, that small-scale water inclusions are the main reason for the typical scattering observed in GPR data for temperate glaciers.

Related to the above, it is conceivable that other, non-considered englacial features may contribute to the scattering

too. Such features could include internal ice structures such as deep crevasses, air voids or moraine material (e.g. rocks) buried within the ice. While such rock inclusions could be of similar size to the water inclusions we considered (diameters ranging from a few millimeters to a few meters), we note that the permittivity of rock ($\epsilon \sim 3$–6) is much closer to the one of ice ($\epsilon \sim 3.2$) than it is to the one of water ($\epsilon \sim 80$; see Tab. 2). This means that the back-scattered energy from a signal originating from rocks is expected to be much weaker than the one from water inclusions. Moreover, the typical pattern of moraines and crevasses at the surface of a glacier, i.e. the fact that such features follow a rather clear spatial distribution, suggests that moraine materials and englacial crevasses are likely less ubiquitous than water inclusions. Although air also has a permittivity that is more similar to ice than water (for air, $\epsilon \sim 1$), its radar velocity is much faster. This causes air voids to produce strong hyperbolas (Nobes, 2017). However, air voids are assumed to be mostly water-filled in temperate ice, or close by ice overburden pressure. Combined, these three arguments let us argue that although englacial crevasses, air voids and rock inclusions might influence the GPR signal, they are very unlikely to be the main source of scattering.

5. Conclusions

In this study, we used numerical modeling of GPR signals to characterize the influence that a wet snowpack, a heterogeneous ice permittivity, and distributed water inclusions have on GPR data acquired on temperate glaciers at 25 MHz. We showed that the presence of wet snow and heterogeneous ice permittivity are insufficient to explain the strong signal scattering often observed in the field, and instead suggest that englacial water inclusions are the main cause for such scattering.

In terms of practical implications, our results confirm that GPR surveys aiming at estimating subglacial characteristics of temperate glaciers are best conducted in winter, when englacial water contents are generally low and the related scattering is suppressed. In such water-free conditions, temperate ice can have a GPR signature that is similar to the one of cold ice. This implies that distinguishing between cold and temperate ice through GPR surveys – as sometimes is done in the literature – bares some pitfalls: while the presence of substantial scattering in the GPR signal can be interpreted as indicative for the presence of water and thus temperate ice, the absence of such scattering is indeed indicative for low water contents but these might occur for both temperate and cold ice. Stated differently: an area free of scatterers is a necessary but not a sufficient condition for interpreting a given ice portion as being cold.

Our numerical simulations also indicate that a bulk LWC of 0.2 %, associated to decimeter-scale water inclusions, is already sufficient to mask bedrock reflections through signal attenuation. The value is in the range of field-based LWC observations, thus explaining why real-world GPR data on temperate ice often fail to detect the bedrock. Our numerical experiments also showed that the GPR signal is sensitive to heterogeneous distributions of water inclusions. In particular, glacier sections with locally low LWC can be far less affected by scattering than sections with high LWC. This gives rise to individual sections that are 'transparent' to the GPR signal, i.e. sections with strong signal reflections from the targeted objects. Finally, we showed that the distribution of small scatterers has less of an impact on target detectability that the distribution of large scatterers. Overall, our results contribute to a better understanding and interpretability of GPR signals over temperate ice.

References

Bamber J (1988) Enhanced radar scattering from water inclusions in ice. *Journal of Glaciology* **34**(118), 293–296. doi: 10.3189/S0022143000007048

Barrett B, Murray T, Clark R and Matsuoka K (2008) Distribution and character of water in a surge-type glacier revealed by multifrequency and multi-polarization ground-penetrating radar. *Journal of Geophysical Research: Earth Surface* **113**(F4), F04011. doi: 10.1029/2007JF000972

Bauder A and 5 others (2018) Winter accumulation measurements on alpine glaciers using ground penetrating radar. In *2018 17th International Conference on Ground Penetrating Radar (GPR)*. Rapperswil, Switzerland: IEEE, pp. 1–5. doi: 10.1109/ICGPR.2018.8441559

Berenger JP (1996) Perfectly matched layer for the FDTD solution of wave-structure interaction problems. *IEEE Transactions on antennas and propagation* **44**(1), 110–117. doi: 10.1109/8.477535

Björnsson H and 6 others (1996) The thermal regime of sub-polar glaciers mapped by multi-frequency radio-echo sounding. *Journal of Glaciology* **42**(140), 23–32. doi: 10.3189/S0022143000030495

Blatter H and Hutter K (1991) Polythermal conditions in arctic glaciers. *Journal of Glaciology* **37**(126), 261–269. doi: 10.3189/S0022143000007279

Bohleber P, Wagner N and Eisen O (2012) Permittivity of ice at radio frequencies: Part ii. artificial and natural polycrystalline ice. *Cold Regions Science and Technology* **83**, 13–19. doi: 10.1016/j.coldregions.2012.05.010

Bradford JH, Nichols J, Mikesell TD and Harper JT (2009) Continuous profiles of electromagnetic wave velocity and water content in glaciers: an example from bench glacier, Alaska, USA. *Annals of Glaciology* **50**(51), 1–9. doi: 10.3189/172756409789097540

Campbell S and 7 others (2012) Melt regimes, stratigraphy, flow dynamics and glaciochemistry of three glaciers in the Alaska range. *Journal of Glaciology* **58**(207), 99–109. doi: 10.3189/2012JoG10J238

Catania GA, Neumann TA and Price SF (2008) Characterizing englacial drainage in the ablation zone of the Greenland ice sheet. *Journal of Glaciology* **54**(187), 567–578. doi: 10.3189/002214308786570854

Church G, Grab M, Schmelzbach C, Bauder A and Maurer H (2020) Monitoring the seasonal changes of an englacial conduit network using repeated ground-penetrating radar measurements. *The Cryosphere* **14**(10), 3269–3286. doi: 10.5194/tc-14-3269-2020

Coleou C, Lesaffre B, Brzoska JB, Ludwig W and Boller E (2001) Three-dimensional snow images by x-ray microtomography. *Annals of glaciology* **32**, 75–81. doi: 10.3189/172756401781819418

Cuffey KM and Paterson WSB (2010) *The physics of glaciers*. Oxford, UK: Butterworth-Heinemann Publications.

Davis JL and Annan AP (1989) Ground-penetrating radar for high-resolution mapping of soil and rock stratigraphy 1. *Geophysical prospecting* **37**(5), 531–551. doi: 10.1111/j.1365-2478.1989.tb02221.x

Evans S (1965) Dielectric properties of ice and snow–a review. *Journal of Glaciology* **5**(42), 773–792. doi: 10.3189/S0022143000018840

Fountain AG and Walder JS (1998) Water flow through temperate glaciers. *Reviews of Geophysics* **36**(3), 299–328. doi: 10.1029/97RG03579

Fujita S, Mae S and Matsuoka T (1993) Dielectric anisotropy in ice Ih at 9.7 GHz. *Annals of Glaciology* **17**, 276–280. doi: 10.3189/S0260305500012969

Garambois S, Legchenko A, Vincent C and Thibert E (2016) Ground-penetrating radar and surface nuclear magnetic resonance monitoring of an englacial water-filled cavity in the polythermal glacier of Tête Rousse. *Geophysics* **81**(1), WA131–WA146. doi: 10.1190/geo2015-0125.1

Gerbi C and 9 others (2021) Microstructures in a shear margin: Jarvis glacier, Alaska. *Journal of Glaciology* **67**(266), 1163–1176. doi: 10.1017/jog.2021.62

Glen J and Paren J (1975) The electrical properties of snow and ice. *Journal of Glaciology* **15**(73), 15–38. doi: 10.3189/S0022143000034249

Goff JA and Holliger K (2012) *Heterogeneity in the crust and upper mantle: nature, scaling, and seismic properties.* New York: Springer Science & Business Media.

Grab M and 8 others (2018) Ice volume estimates of Swiss glaciers using helicopter-borne GPR–an example from the Glacier de la Plaine Morte. In *2018 17th International Conference on Ground Penetrating Radar (GPR).* Rapperswil, Switzerland: IEEE, pp. 1–4. doi: 10.1109/ICGPR.2018.8441613

Grab M and 9 others (2021) Ice thickness distribution of all Swiss glaciers based on extended ground-penetrating radar data and glaciological modeling. *Journal of Glaciology* **67**(266), 1074–1092. doi: 10.1017/jog.2021.55

Gräff D and Walter F (2021) Changing friction at the base of an alpine glacier. *Scientific reports* **11**(1), 1–10. doi: 10.1038/s41598-021-90176-9

Granlund N, Lundberg A and Gustafsson D (2010) Laboratory study of the influence of salinity on the relationship between electrical conductivity and wetness of snow. *Hydrological processes* **24**(14), 1981–1984. doi: 10.1002/hyp.7659

Griessinger N, Mohr F and Jonas T (2018) Measuring snow ablation rates in alpine terrain with a mobile multioffset ground-penetrating radar system. *Hydrological Processes* **32**(21), 3272–3282. doi: 10.1002/hyp.13259

Gusmeroli A, Jansson P, Pettersson R and Murray T (2012) Twenty years of cold surface layer thinning at Storglaciären, Sub-arctic Sweden, 1989–2009. *Journal of Glaciology* **58**(207), 3–10. doi: 10.3189/2012JoG11J018

Hamran S, Aarholt E, Hagen JO and Mo P (1996) Estimation of relative water content in a sub-polar glacier using surface-penetration radar. *Journal of Glaciology* **42**(142), 533–537. doi: 10.3189/S0022143000003518

Hertrich M and Walbrecker J (2008) The potential of surface-nmr to image water in permafrost and glacier ice. In *EGU General Assembly*, Vienna, Austria, Vol. 10, EGU2008-A-06663.

Hertrich M, Braun M, Gunther T, Green AG and Yaramanci U (2007) Surface nuclear magnetic resonance tomography. *IEEE Transactions on Geoscience and Remote Sensing* **45**(11), 3752–3759. doi: 10.1109/TGRS.2007.903829

Hodge SM (1976) Direct measurement of basal water pressures: a pilot study. *Journal of Glaciology* **16**(74), 205–218. doi: 10.3189/S0022143000031543

Holmlund P (1988) Internal geometry and evolution of Moulins, Storglaciären, Sweden. *Journal of Glaciology* **34**(117), 242–248. doi: 10.3189/S0022143000032305

Iken A, Fabri K and Funk M (1996) Water storage and subglacial drainage conditions inferred from borehole measurements on Gornergletscher, Galais, Switzerland. *Journal of Glaciology* **42**(141), 233–248. doi: 10.3189/S0022143000004093

Jezek KC, Clough JW, Bentley CR and Shabtaie S (1978) Dielectric permittivity of glacier ice measured in situ by radar wide-angle reflection. *Journal of Glaciology* **21**(85), 315–329. doi: 10.3189/S0022143000033505

Johari GP and Charette P (1975) The permittivity and attenuation in polycrystalline and single-crystal ice Ih at 35 and 60 Mhz. *Journal of Glaciology* **14**(71), 293–303. doi: 10.3189/S002214300002178X

Kovacs A, Gow AJ and Morey RM (1995) The in-situ dielectric constant of polar firn revisited. *Cold Regions Science and Technology* **23**(3), 245–256. doi: 10.1016/0165-232X(94)00016-Q

Kunz KS and Luebbers RJ (1993) *The finite difference time domain method for electromagnetics.* Boca Raton, FL: CRC Press.

Langhammer L, Rabenstein L, Bauder A and Maurer H (2017) Ground-penetrating radar antenna orientation effects on temperate mountain glaciers. *Geophysics* **82**(3), H15–H24. doi: 10.1190/geo2016-0341.1

Legchenko A and 6 others (2011) Three-dimensional magnetic resonance imaging for groundwater. *New Journal of Physics* **13**(2), 025022. doi: 10.1088/1367-2630/13/2/025022

Macheret YY and Glazovsky AF (2000) Estimation of absolute water content in Spitsbergen glaciers from radar sounding data. *Polar Research* **19**(2), 205–216. doi: 10.3402/polar.v19i2.6546

Macheret YY, Moskalevsky MY and Vasilenko E (1993) Velocity of radio waves in glaciers as an indicator of their hydrothermal state, structure and regime. *Journal of Glaciology* **39**(132), 373–384. doi: 10.3189/S0022143000030495

Margrave GF and Lamoureux MP (2019) *Numerical methods of exploration seismology: With algorithms in MATLAB®.* Cambridge, England: Cambridge University Press.

Moore J and 8 others (1999) High-resolution hydrothermal structure of Hansbreen, Spitsbergen, mapped by ground-penetrating radar. *Journal of Glaciology* **45**(151), 524–532. doi: 10.3189/S0022143000001386

Murray T, Stuart GW, Fry M, Gamble NH and Crabtree MD (2000) Englacial water distribution in a temperate glacier from surface and borehole radar velocity analysis. *Journal of Glaciology* **46**(154), 389–398. doi: 10.3189/172756500781833188

Navarro F and Eisen O (2009) 11 ground-penetrating radar in glaciological applications. In *Remote sensing of glaciers: Techniques for topographic, spatial and thematic mapping of glaciers.* London, England: Taylor & Francis, pp. 195–229. doi: 10.1201/b10155-12

Nobes DC (2017) Ground penetrating radar response from voids: A demonstration using a simple model. *Ndt & E International* **91**, 47–53. doi: 10.1016/j.ndteint.2017.05.007

Özdemir C, Demirci Ş, Yiğit E and Yilmaz B (2014) A review on migration methods in b-scan ground penetrating radar imaging. *Mathematical Problems in Engineering* **2014**, 280738. doi: 10.1155/2014/280738

Pettersson R, Jansson P and Blatter H (2004) Spatial variability in water content at the cold-temperate transition surface of the polythermal Storglaciären, Sweden. *Journal of Geophysical Research: Earth Surface* **109** (F2), F02009. doi: 10.1029/2003JF000110

Plewes LA and Hubbard B (2001) A review of the use of radio-echo sounding in glaciology. *Progress in Physical Geography* **25**(2), 203–236. doi: 10.1177/0309133301025002

Pohle A, Werder MA, Gräff D and Farinotti D (2022) Characterising englacial R-channels using artificial moulins. *Journal of Glaciology* **68** (271), 879–890. doi: 10.1017/jog.2022.4

Rada C and Schoof C (2018) Channelized, distributed, and disconnected: subglacial drainage under a valley glacier in the Yukon. *The Cryosphere* **12**(8), 2609–2636. doi: 10.5194/tc-12-2609-2018

Raymond C and Harrison W (1975) Some observations on the behavior of the liquid and gas phases in temperate glacier ice. *Journal of Glaciology* **14**(71), 213–233. doi: 10.3189/S0022143000021717

Reynolds JM (2011) *An introduction to applied and environmental geophysics.* Hoboken, NJ: John Wiley & Sons.

Robin GdQ, Evans S and Bailey JT (1969) Interpretation of radio echo sounding in polar ice sheets. *Philosophical Transactions of the Royal Society of London. Series A, Mathematical and Physical Sciences* **265** (1166), 437–505. doi: 10.1098/rsta.1969.0063

Rutishauser A, Maurer H and Bauder A (2016) Helicopter-borne ground-penetrating radar investigations on temperate alpine glaciers: a comparison of different systems and their abilities for bedrock mapping. *Geophysics* **81** (1). WA119–WA129. doi: 10.1190/geo2015-0144.1

Schneider JB (2010) Understanding the finite-difference time-domain method. *School of electrical engineering and computer science Washington State University.* Pullman, WA: Washington State University, Vol. 28.

Schroeder DM and 9 others (2020) Five decades of radioglaciology. *Annals of Glaciology* **61**(81), 1–13. doi: 10.1017/aog.2020.11

Smith BE and Evans S (1972) Radio echo sounding: absorption and scattering by water inclusion and ice lenses. *Journal of Glaciology* **11**(61), 133–146. doi: 10.3189/S0022143000022541

Tiuri M, Sihvola A, Nyfors E and Hallikaiken M (1984) The complex dielectric constant of snow at microwave frequencies. *IEEE Journal of Oceanic Engineering* **9**(5), 377–382. doi: 10.1109/JOE.1984.1145645

Vallon M, Petit JR and Fabre B (1976) Study of an ice core to the bedrock in the accumulation zone of an alpine glacier. *Journal of Glaciology* **17**(75), 13–28. doi: 10.3189/S0022143000030677

Warren C, Giannopoulos A and Giannakis I (2016) gprMax: open source software to simulate electromagnetic wave propagation for ground penetrating radar. *Computer Physics Communications* **209**, 163–170. doi: 10.1016/j.cpc.2016.08.020

Watts RD and England AW (1976) Radio-echo sounding of temperate glaciers: ice properties and sounder design criteria. *Journal of Glaciology* **17**(75), 39–48. doi: 10.3189/S0022143000030707

Werder MA, Schuler TV and Funk M (2010) Short term variations of tracer transit speed on alpine glaciers. *The Cryosphere* **4**(3), 381–396. doi: 10.5194/tc-4-381-2010

Woodward J and Burke MJ (2007) Applications of ground-penetrating radar to glacial and frozen materials. *Journal of Environmental & Engineering Geophysics* **12**(1), 69–85. doi: 10.2113/JEEG12.1.69